

Article

Compressive and Tensile Behavior of High-Ductility Alkali-Activated Composites with Polyethylene Terephthalate Powder

Fei Meng¹, Shen Luo¹, Jingxian Sun¹, Cheng Zhang¹, Leilei Xu¹, Yankun Du¹, Junfeng Zeng² and Yongchang Guo^{2,*}

¹ Zhongshan Power Supply Bureau, Guangdong Power Grid Co., Ltd., China Southern Power Grid Co., Ltd., Zhongshan 525000, China; blackstar_002@sina.cn (F.M.); zsluocong@163.com (S.L.); 1290025427@163.com (J.S.); 314355@163.com (C.Z.); 13924971515@139.com (L.X.); 18685441709@163.com (Y.D.)

² School of Civil and Transportation Engineering, Guangdong University of Technology, Guangzhou 510006, China; 13580510012@139.com

* Correspondence: guoyc@gdut.edu.cn; Tel.: +86-203-9322-538

Abstract: Researchers have been engaged in the study of high-ductility concrete (HDC) due to its excellent ductility and cracking control ability. This study combines the concepts of HDC and alkali-activated composites (AAC) to develop high-ductility alkali-activated composites (HDAAC) using polyethylene terephthalate (PET) powder. Experimental investigations were conducted to assess the compressive and tensile properties of HDAAC, focusing on the impact of varying PET powder content (0%, 15%, 30%, and 45%) and fly ash/slag ratios (FA/GGBS, 6:4, 7:3, and 8:2). The results indicated that the compressive strength of HDAAC ranged from approximately 30 MPa to about 100 MPa, with the specimens maintaining good integrity after axial compression failure due to the bridging action of PE fibers. The replacement of quartz powder (QP) with PET powder slightly decreased the compressive strength and elastic modulus of HDAAC, albeit mitigating its brittleness under compression. An increase in GGBS content enhanced the compressive strength and elastic modulus of HDAAC due to the increased formation of the C-A-S-H reaction products, leading to reduced porosity and a denser microstructure. Under axial tension, HDAAC exhibited typical multiple-cracking behavior with significant pseudo-strain hardening. Increases in the PET content and FA/GGBS ratio resulted in finer cracks, indicating excellent crack control and deformation capabilities. The initial cracking strength, tensile strength, and ultimate tensile strain ranged from 3.0 MPa to 4.6 MPa, 4.2 MPa to 8.2 MPa, and 4.1% to 7.2%, respectively. Despite a decrease in the initial cracking strength and tensile strength with higher PET content, the ultimate tensile strain of HDAAC slightly increased. Observations under a scanning electron microscope revealed a distinct interfacial transition zone near the PET powder, leading to poor bonding with the alkali-activated matrix. In contrast, QP dissolved on the surface in highly alkaline environments, forming better interface properties. These variations in interface properties can be used to interpret the variations in the mechanical performance of HDAAC.

Keywords: alkali-activated composites (AAC); high ductility; polyethylene terephthalate (PET) powder; tensile behavior



Citation: Meng, F.; Luo, S.; Sun, J.; Zhang, C.; Xu, L.; Du, Y.; Zeng, J.; Guo, Y. Compressive and Tensile Behavior of High-Ductility Alkali-Activated Composites with Polyethylene Terephthalate Powder. *Buildings* **2024**, *14*, 1399. <https://doi.org/10.3390/buildings14051399>

Academic Editor: Antonio Caggiano

Received: 10 April 2024

Revised: 1 May 2024

Accepted: 2 May 2024

Published: 13 May 2024



Copyright: © 2024 by the authors. Licensee MDPI, Basel, Switzerland. This article is an open access article distributed under the terms and conditions of the Creative Commons Attribution (CC BY) license (<https://creativecommons.org/licenses/by/4.0/>).

1. Introduction

Improving the ductility and lifespan of building structures poses a persistent challenge for researchers in the engineering field globally [1,2]. At the material level, the discovery by Romualdi and Batson [3] that steel fibers can significantly reduce cement brittleness spurred scholars to explore various fiber-reinforced cementitious materials [4–9]. With further research, the performance of fiber-reinforced concrete has been continuously improved, leading to the emergence of high-ductility concrete (HDC) characterized by superior tensile ductility. After optimizing the interaction between the matrix and fibers

based on micromechanics and fracture mechanics, HDC can exhibit tensile ductility and crack control capacities far superior to those of ordinary concrete. Since Li and Leung laid the theoretical foundation for this type of material [10,11], research in this area has made progress worldwide, resulting in different terminology in various regions, such as engineered cementitious composites (ECC), ultra-high-toughness cementitious composites (UHTCC), and high-ductility concrete (HDC) [4,12–14]. Generally, the volume fraction of short fibers in HDC does not exceed 2.5%, exhibiting the characteristics of steady-state cracking, multiple cracking, and strain hardening, with an ultimate tensile strain that can stably reach 3% or more. Meanwhile, with the increasing worldwide emphasis on green and low-carbon development models recently, scholars have begun exploring ways to mitigate the high/ultra-high cement consumption associated with HDC, especially in high-strength/ultra-high-strength HDC, thereby reducing the significant CO₂ emissions generated by the cement production process. Cement production reportedly contributes to a global CO₂ emissions increase of at least 5–8% [15], which is of great concern given that the seriousness of climate issues is becoming increasingly evident. Hence, there is a pressing need for low-carbon, energy-efficient cementitious alternatives to replace cement. In this regard, alkali-activated materials (AAMs) have garnered significant attention among scholars.

In 1908, German scholar Hans [16] discovered the reactivity between alkaline materials and aluminum and silicate solid materials, yielding solid materials akin to hardened silicate cement. It was not until the early 1980s that French scholar J. Davidovits applied for patents related to these materials, naming them “geopolymers.” Geopolymers, categorized among AAMs, primarily encompass low-calcium or non-calcium systems like fly ash (FA) and clay [17,18]. Additionally, AAMs include high-calcium systems like ground-granulated blast furnace slag (GGBS) [18,19]. AAMs are novel cementitious systems produced from natural minerals containing aluminosilicate substances (e.g., kaolin) and industrial solid waste (e.g., FA, GGBS, steel slag, red mud, various tailings) as primary ingredients [20,21]. As raw materials are predominantly sourced from industrial waste, AAMs production consumes 70% less energy than cement production and reduces the total pollution by 90% [22]. Consequently, AAMs emerge as an advanced green building material with significant development potential.

In exploring the concepts of HDC and AAMs, researchers have developed a range of high-ductility alkali-activated composites (HDAAC), also called strain-hardening AAC (SHAAC), and scrutinized their mechanical properties [23–29]. Kumar, Sekhar Das, Lao, Alrefaei, and Dai [23] experimentally revealed a direct correlation between the interfacial tensile bonding strength of HDAAC and the S/B ratio. Lee, Oh, Banthia, and Yoo [24] achieved compressive strength exceeding 100 MPa in SHAAC by utilizing slag and glass powder, highlighting the efficacy of higher-aspect-ratio fibers in enhancing SHAAC's tensile performance. Nguyễn, Lương, Choi, Ranade, Li, and Lee [25] realized a tensile strain capacity of 13.7% and tensile strength of 6.8 MPa with a sodium metasilicate pentahydrate to sodium hydroxide (SMP/SH) ratio of 1.5 in their study. Their chemical analysis confirmed that C-(N)-A-S-H and N-A-S-H were the primary products of fly ash-based SHAAC. Additionally, Peng, Zheng, Pan, Yang, Lin, Lai, Wu, and Zhu [27] developed an SHAAC by employing polyoxymethylene fibers instead of PE fibers, resulting in significantly lower costs, carbon emissions, and energy consumption compared to HDC.

From an environmental perspective, researchers frequently turn to waste-derived aggregates as alternatives to natural sand and gravel, aiming to alleviate resource scarcities and tackle the challenges posed by difficult-to-handle solid waste. The extensive production of plastic products, like polyethylene terephthalate (PET) for beverage bottles, has resulted in the significant accumulation of plastic waste, releasing harmful compounds into the environment over time. Studies have suggested that repurposing plastics as aggregates could help to mitigate this issue, offering a sustainable solution [30–32]. While there is scant literature on the use of plastic aggregates in HDC, research on conventional concrete provides some groundwork. Typically, the incorporation of plastic aggregates diminishes

concrete's compressive strength, with the reduction correlating positively with the plastic content [32–34]. The reduction in concrete's compressive strength upon introducing plastic aggregates can be attributed to several factors. Firstly, compared to natural aggregates, plastic aggregates exhibit weaker bonding with the cement matrix. Secondly, their lower stiffness and strength lead to stress concentration at the interfaces, resulting in crack formation around the plastic aggregates. Additionally, plastic's hydrophobic nature impedes water movement, slowing down cement's hydration [35,36]. Furthermore, the inclusion of plastic aggregates increases concrete's fracture energy and characteristic length. For instance, increasing the plastic volume from 0% to 40% raised the fracture energy from 89.9 N/m to 98.8 N/m, and the characteristic length of concrete increased by approximately 77% [37]. The effect on concrete's fracture performance may also impact the tensile behavior of HDC, given that HDC's tensile performance is chiefly influenced by factors like the matrix fracture toughness and fiber-bridging strength.

This study introduced HDAAC with PET powder and experimentally investigated the effect of varying the PET powder content and FA/GGBS ratios on the compressive and tensile properties of the HDAAC. Through axial compression tests and axial tension tests, the study investigated the failure modes, stress–strain curves, and changes in the characteristic parameters of the compressive performance (e.g., compressive strength, elastic modulus) and tensile performance (e.g., tensile strength, ultimate tensile strain, and strain energy) under different PET powder content and FA/GGBS ratios. Furthermore, scanning electron microscopy (SEM) was utilized to validate the influence of the PET powder and FA/GGBS ratios on the experimental results from a microscopic perspective. By elucidating these aspects, this study contributes to a deeper understanding of the mechanical behavior of HDAAC with PET powder, offering insights into its potential applications and paving the way for future research endeavors in this field.

2. Experimental Program

2.1. Materials and Mix Proportion

HDAAC were produced from precursors, fine aggregates, alkali activators, retarders, fibers, and water. The particle size distribution of the precursors and fine aggregates is illustrated in Figure 1, consisting of S105 GGBS and Class F FA, with the X-ray diffraction (XRD) results shown in Figure 2. The chemical compositions of GGBS and FA, analyzed via X-ray fluorescence (XRF), are presented in Table 1. The fine aggregates consisted of quartz powder (QP) and PET powder, with QP ranging from 76 μm to 150 μm and having a density of 2.65 g/cm^3 . The PET powder, sourced mainly from Dongguan Guangyuan Plastic Co., Ltd., had a diameter of around 106 μm and a density of 1.68 g/cm^3 . The macroscopic morphology and scanning electron microscopy (SEM) image of the PET powder are shown in Figure 3. PET, a common plastic used in various products, poses environmental challenges due to its poor biodegradability [38]. Recycling waste products into recycled aggregates to replace natural aggregates is a common method to address non-biodegradable waste, reduce costs, and achieve enhanced sustainability.

Table 1. Chemical composition of GGBS and FA (unit: wt%).

	CaO	SiO ₂	Al ₂ O ₃	SO ₃	Fe ₂ O ₃	MgO	TiO ₂	Others	LOI (%)
GGBS	34.00	34.50	17.70	1.64	1.03	6.01	/	5.12	0.84
FA	4.01	53.97	31.15	2.20	4.16	1.01	1.13	2.37	4.60

Note: LOI denotes loss on ignition.

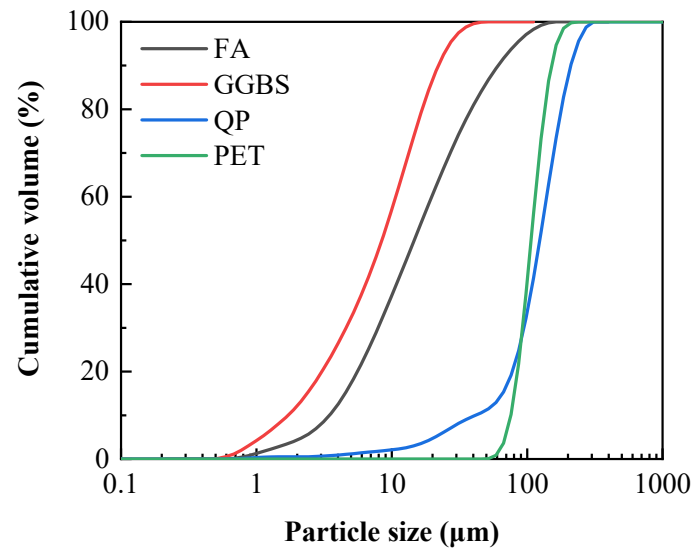


Figure 1. Particle size distributions of raw materials.

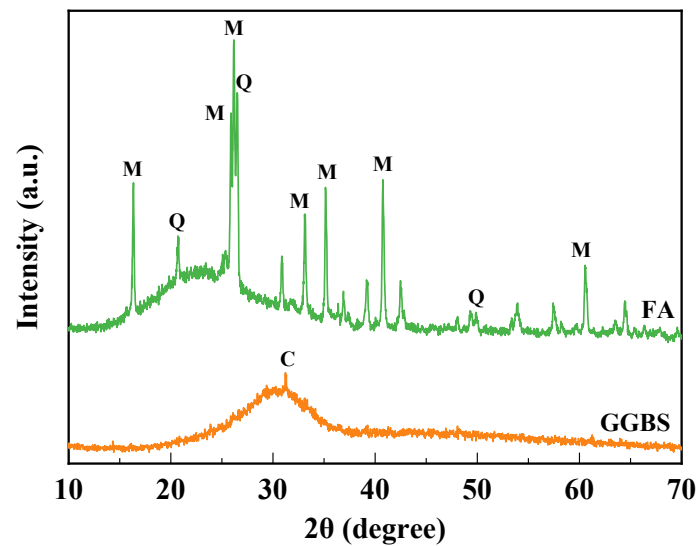
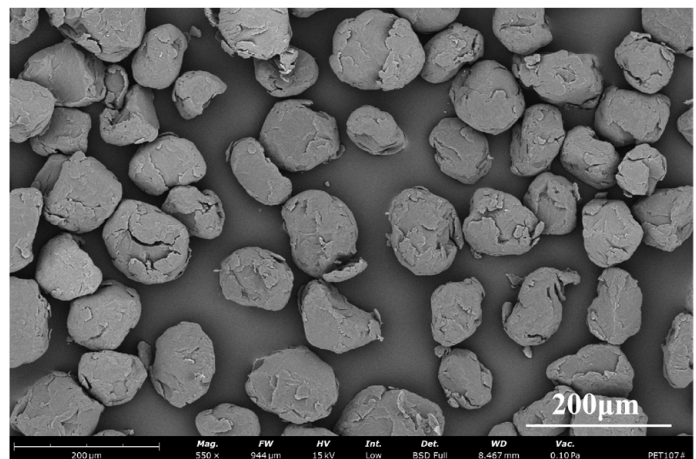


Figure 2. XRD patterns of FA and GGBS (M = mullite, Q = quartz, C = $\text{Ca}_3\text{Al}_2\text{Si}_2$).



(a)



(b)

Figure 3. PET powder: (a) macroscopic morphology, (b) SEM image.

The alkali activator solution (AAS) was prepared by mixing a 2.25 modulus sodium silicate (SS) solution with a 10 mol/L SH solution at a 2:1 ratio. The method is as follows. First, prepare 1000 mL of SH solution. Start by weighing 400 g of solid SH and dissolving it in water with rapid stirring. Seal the beaker with a plastic film to prevent evaporation, and allow it to cool. Once cooled, transfer the solution to a volumetric flask and dilute it with water to reach a final volume of 1000 mL. Then, add SS solution in proportion to obtain the required AAS. Afterwards, reseal the container, and allow it to cool for at least 24 h before using it for experimental casting. In this study, the SS solution was a colorless, transparent, viscous liquid with a modulus of 2.25 and a density of 1.5 g/cm³. The ratio of m(SiO₂)/m(Na₂O)/m(H₂O) was 29.99:13.75:56.26. The SH used in the study was a white granular solid with purity of ≥96%. Meanwhile, barium chloride (BaCl₂), with purity of 99%, was utilized as the retarder at a fixed dosage of 1% of the cementitious material. Ultra-high-molecular-weight polyethylene fibers were adopted to provide strong fiber-bridging strength, conducive to enhancing the pseudo-strain hardening behavior and multiple cracking phenomena. The fiber parameters are detailed in Table 2.

Table 2. Relevant parameters of PE fibers.

Length (mm)	Diameter (mm)	Tensile Strength (MPa)	Elastic Modulus (GPa)	Density (g/cm ³)	Elongation (%)
12	20	2500	120	0.97	3.7

Table 3 outlines the mix proportions of the HDAAC used in this study, divided into three groups, M1, M2, and M3, representing matrices with FA/GGBS ratios of 6:4, 7:3, and 8:2, respectively. Each group included four PET powder volume replacement rates (0%, 15%, 30%, 45%). Additionally, the dosages of AAS, water, and BaCl₂ were fixed at 40%, 10%, and 1% of the precursors, respectively, while the PE fiber content remained fixed at 2% vol.

Table 3. Mix proportions.

Group	Mix ID	FA ¹	GGBS ²	QP ³	PET ⁴	AAS ⁵	Water	BaCl ₂	PE ⁶
M1	M1-P0	0.60	0.40	0.20	0.00	0.40	0.10	0.01	2.0% (Vol.)
	M1-P15			0.18	0.02				
	M1-P30			0.16	0.04				
	M1-P45			0.14	0.06				
M2	M2-P0	0.70	0.30	0.20	0.00	0.40	0.10	0.01	2.0% (Vol.)
	M2-P15			0.18	0.02				
	M2-P30			0.16	0.04				
	M2-P45			0.14	0.06				
M3	M3-P0	0.80	0.20	0.20	0.00	0.40	0.10	0.01	2.0% (Vol.)
	M3-P15			0.18	0.02				
	M3-P30			0.16	0.04				
	M3-P45			0.14	0.06				

¹ fly ash; ² ground granulated blast furnace slag; ³ quartz powder; ⁴ recycled polyethylene terephthalate powder; ⁵ alkali-activated solution; ⁶ polyethylene fibers.

2.2. Specimens and Preparation

As illustrated in Figure 4, the experiment in this study comprised axial compressive and tensile tests. As per ASTM-C469 [39], cylindrical specimens measuring Φ50 mm × 100 mm were utilized to investigate the compressive performance of HDAAC. Meanwhile,

the axial tensile tests conformed to the JSCE [40], employing dumbbell-shaped specimens measuring 330 mm × 60 mm × 13 mm.

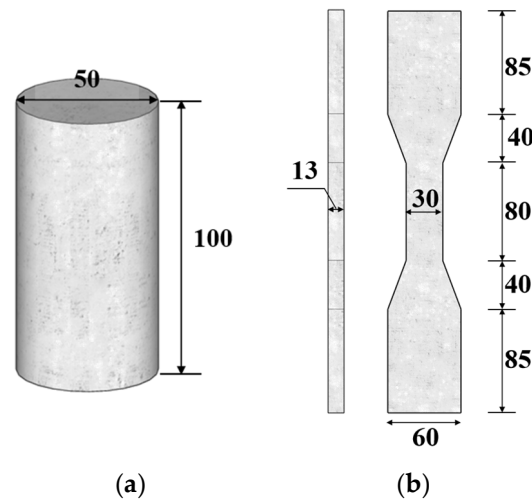


Figure 4. Specimens adopted for (a) cylinder specimen, (b) dumbbell-shaped specimen.

Figure 5 depicts the preparation process of HDAAC. A 30 L planetary mixer with variable speeds was employed. Initially, dry powders (FA, GGBS, QP, and PET powder) and a retarder (BaCl_2) were added, followed by 3 min of low-speed (75 r/min) mixing to ensure uniform blending. Subsequently, while stirring, the AAS was added and mixed at a low speed for 2 min. Additional water was then introduced, and mixing continued at a medium speed (165 r/min) for 1 min. Finally, PE fibers were added during low-speed mixing, ensuring completion within 3 min to prevent the uneven distribution of the fibers. Once mixed, the HDAAC were poured into molds, compacted on a vibrating table, covered with a plastic film, and afterwards cured in the lab for 24 h before demolding. Following this, the specimens underwent 28 days of indoor water immersion for formal testing.

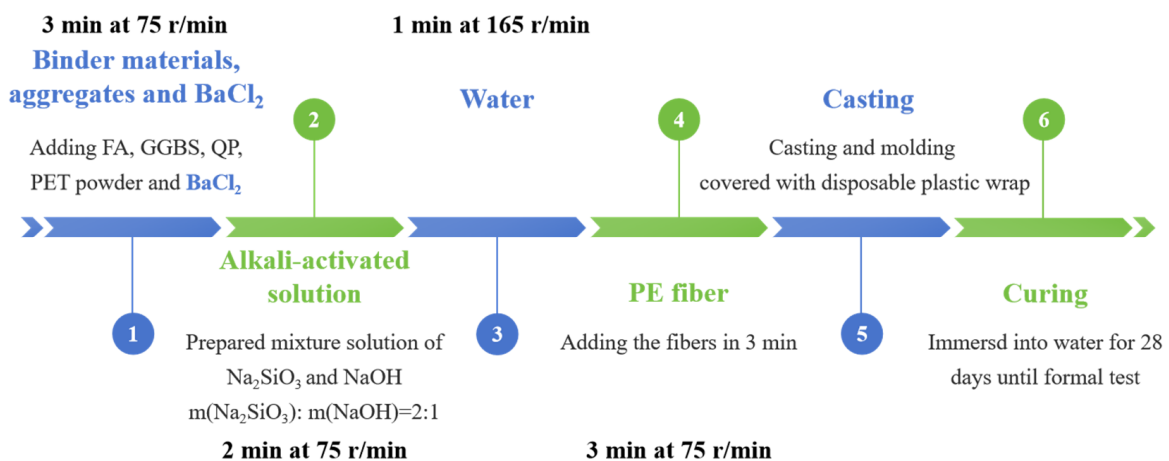


Figure 5. Preparation of HDAAC.

3. Experimental Setup and Procedure

3.1. Axial Compressive Test

According to ASTM C469 [39], cylindrical specimens were used for the axial compression tests in this study, and the test equipment for the axial compression test is depicted in Figure 6. High-strength gypsum of around 80 MPa, according to the manufacturer, was applied for leveling before testing to prevent eccentric loading. The tests were conducted on a machine with a maximum loading capacity of 5000 kN, using a displacement loading

mode of 0.12 mm/min. During loading, the machine measured the load, while two LVDTs measured the axial displacement at the high section of the specimen, as shown in Figure 6. Additionally, two symmetrically distributed strain gauges were adopted to measure the axial strain. Throughout the experiment, data including the load, axial displacement, and strain were collected simultaneously using a high-speed static strain gauge.

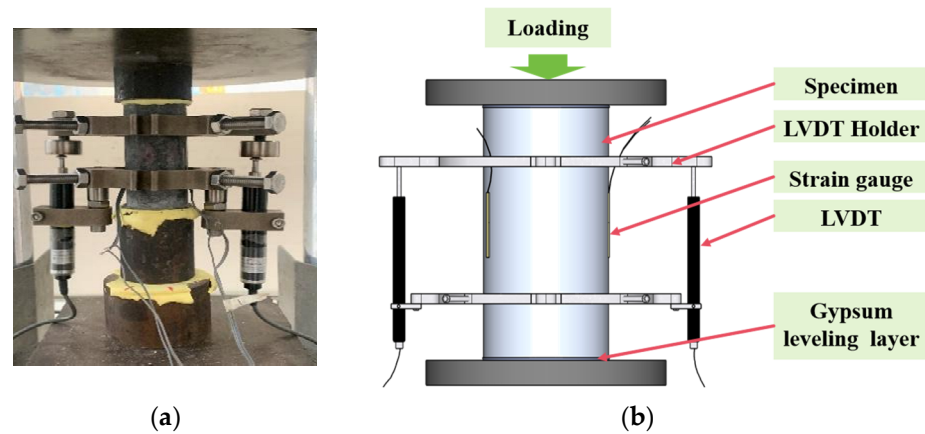


Figure 6. Test equipment for axial compression test: (a) test setup, (b) schematic diagram.

3.2. Axial Tensile Test

Following the guidelines of JSCE [40], dumbbell-shaped specimens were employed for the tensile tests (see Figure 7). Universal joints were installed at both ends of the fixtures to prevent eccentric loading. The tests were conducted on a universal testing machine with a maximum loading capacity of 100 kN, using a displacement loading mode of 0.5 mm/min. Similarly to the axial compression tests, the machine measured the load during loading. Two LVDTs were utilized at both ends of the specimen to measure the axial displacement, focusing on the central 80 mm region. Throughout the experiment, data including the load and axial displacement were collected using a high-speed static strain gauge.

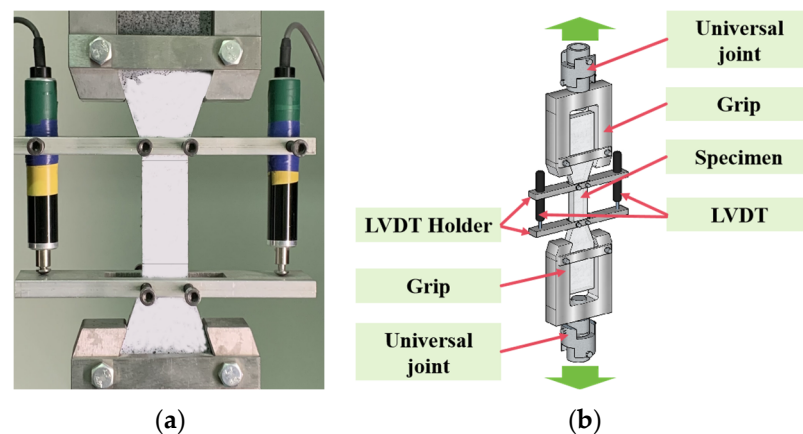


Figure 7. Test equipment for axial tension test: (a) test setup, (b) schematic diagram.

3.3. SEM

Scanning electron microscopy (SEM) tests were conducted in order to characterize the matrix properties. Before microscale testing, specimens were cut for observation. The specimens were polished to obtain smooth and flat observation surfaces, and then coated with a layer of gold spray. Subsequently, the specimen was magnified to approximately 1000 times to observe the microstructure of the SHAAC.

4. Results and Discussion

4.1. Compressive Behavior

4.1.1. Failure Mode

Figure 8 illustrates the failure mode of HDAAC under axial compression. Concrete failure is related to the initiation and propagation of internal microcracks [41]. Typically, cracks begin to initiate and propagate as the loading reaches a certain stage. Subsequently, some cracks start to connect and close with the increasing load, while others propagate slowly. When the accumulated internal energy of the concrete exceeds the energy required for cracking, the cracks undergo unstable propagation, and the concrete gradually collapses.

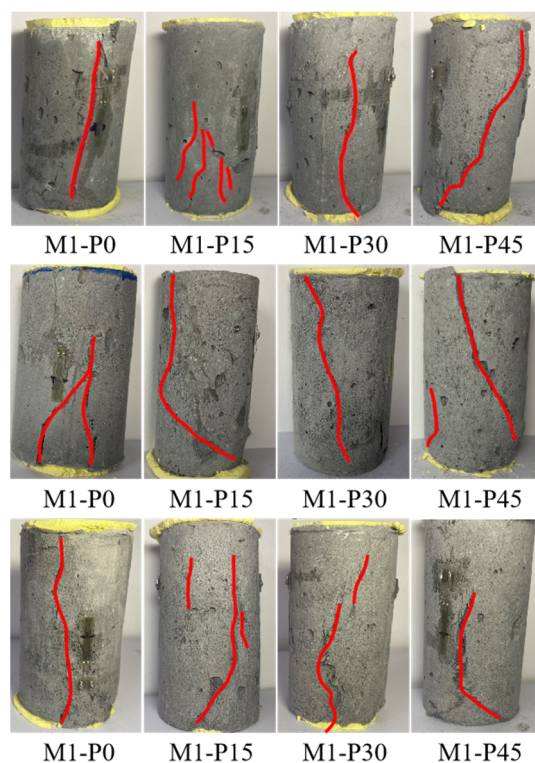


Figure 8. Failure mode of HDAAC under axial compression (with cracks marked in red).

Similar phenomena were observed in the axial compression tests of the HDAAC in this study. However, due to the addition of PE fibers, the HDAAC fractured instead of shattering upon ultimate failure, maintaining relatively good integrity. This was because the high-strength and high-modulus PE fibers could effectively limit the transverse deformation of the specimens [42]. With the increasing PET powder content, some microcracks formed before the specimen's failure, and the angle of the main crack gradually decreased, transitioning from vertical cracks to inclined cracks, as shown in Figure 8. Therefore, increasing the PET powder content in HDAAC may slightly mitigate their inherent brittleness under compression [43]. Additionally, as the FA/GGBS ratio increased, the angle of the main crack decreased, also indicating a reduction in brittleness. These results aligned with existing research findings [44]. However, it should be noted that the sharp expansion of the main crack was observed when the HDAAC reached the peak load during the experiments, indicating that their brittleness under compression conditions remained significant.

4.1.2. Stress–Strain Curves

The axial stress–strain curves of the HDAAC are presented in Figure 9. The curves of the HDAAC continuously rose with the increasing load. Upon reaching the peak load, the curves sharply declined. Subsequently, due to the bridging effect of the PE fibers, the specimens maintained relatively good integrity, and the curves showed a slow and

continuous decline in stress. With the increasing PET powder content, both the slope of the ascending branch of the curves and their peak points decreased, but the rate of stress decreased when the curves reached the peak load. This implied that the compressive strength and elastic modulus of the HDAAC decreased slightly when the PET powder replaced the quartz powder. Meanwhile, the brittleness of the HDAAC was maintained under compression conditions. The decrease in the compressive strength and elastic modulus may have been due to the smooth surface of the PET powder, resulting in loose bonding with the surrounding matrix, thus affecting the compressive strength [45,46]. Moreover, since the PET powder itself was more flexible, its incorporation resulted in increased deformation and a decreased elastic modulus in the HDAAC [47]. Overall, the trend of decreasing compressive performance observed in this study was generally consistent with previous research [43,45–47].

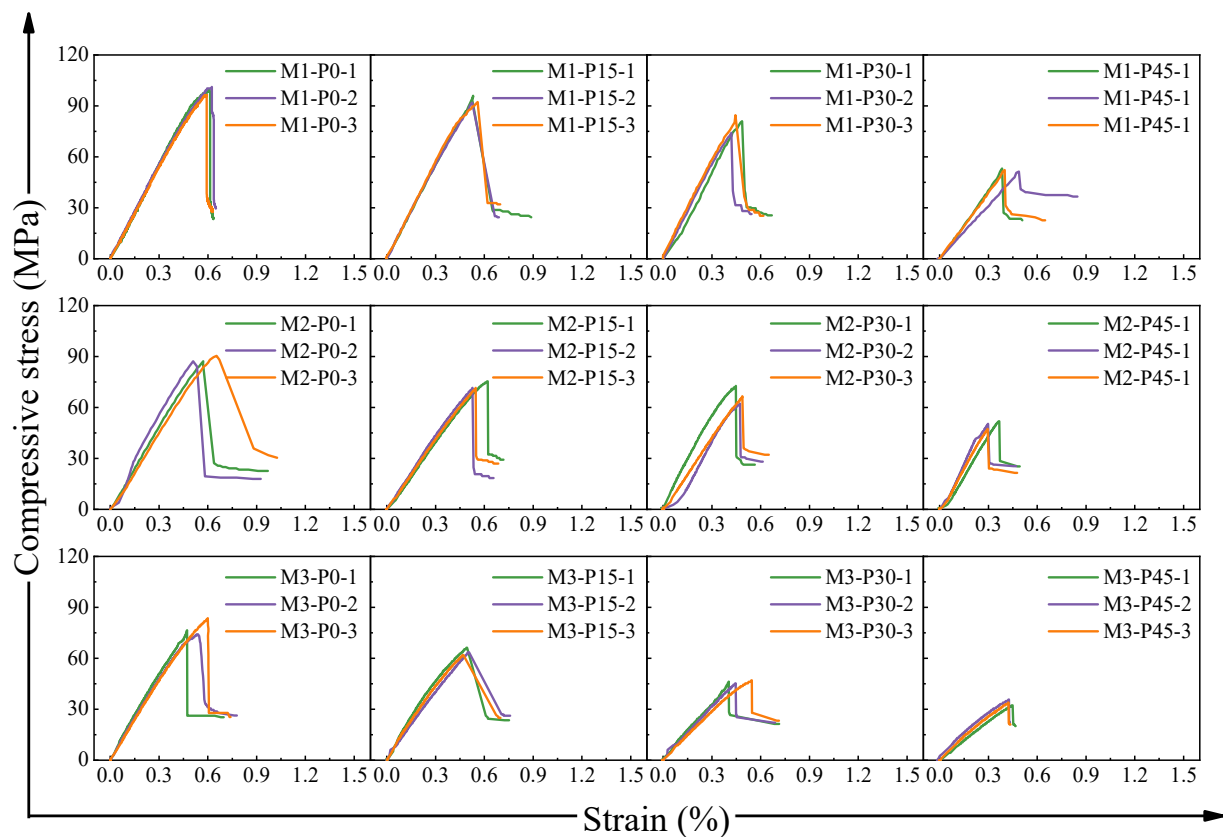


Figure 9. Stress–strain curves of HDAAC under axial compression.

Additionally, with the increase in FA/GGBS, a decrease in both the slope of the ascending branch of the stress–strain curves and their peak points could be observed, indicating a decrease in the compressive strength and elastic modulus. This was because the microstructure of the AAM strongly depended on the FA/GGBS, which significantly affected the mechanical properties. When the slag content was higher, the reaction products mainly consisted of C-A-S-H gel, but when the fly ash content was higher, the reaction products mainly consisted of N-C-A-S-H gel [28]. It has been reported that C-A-S-H gels have a foil-like morphology, while N-C-A-S-H gels show a globular-like morphology [48]. The presence of the C-A-S-H gel had a significant positive effect on the compressive strength and elastic modulus; thus, the compressive strength and elastic modulus of the HDAAC decreased when the FA/GGBS increased [44]. These findings are consistent with previous research on alkali-activated concrete [18,19].

4.1.3. Compressive Strength and Elastic Modulus

Figure 10 presents the variations in the compressive strength and elastic modulus of the HDAAC under different PET powder content and FA/GGBS ratios. Table 4 specifically presents the compressive strength and elastic modulus of the HDAAC. The compressive strength and elastic modulus of the HDAAC ranged from 34.0 MPa to 98.7 MPa and 9.2 GPa to 21.2 GPa, both showing a steady decrease with increasing PET powder content and FA/GGBS ratios. Specifically, taking group M2 as an example, compared to M2-P0, the compressive strength of M2-P15, M2-P30, and M2-P45 decreased by 17.6%, 24.2%, and 43.5%, respectively, while the elastic modulus decreased by 10.3%, 18.2%, and 23.6%, respectively. Some research has found that the compressive strength of PET concrete may be slightly increased when the PET content is low. It is suggested that this is due to the unique shape and flexibility of PET particles, which increase the probability of interlocking between the PET particles on the fracture surface when the load reaches its maximum, thus delaying the failure of concrete [47]. However, in this study, only a continuous decrease in the compressive strength and elastic modulus was observed. On the one hand, this was because the particle size of the PET powder used in this study was much smaller than that used in other studies, resulting in a lower probability of interlocking between the PET particles. On the other hand, the high level of PET powder substitution in this study resulted in weak bonding between the PET and the surrounding matrix, leading to the continuous deterioration of the compressive performance of the HDAAC due to their hydrophobic nature. This was generally consistent with existing research results [45].

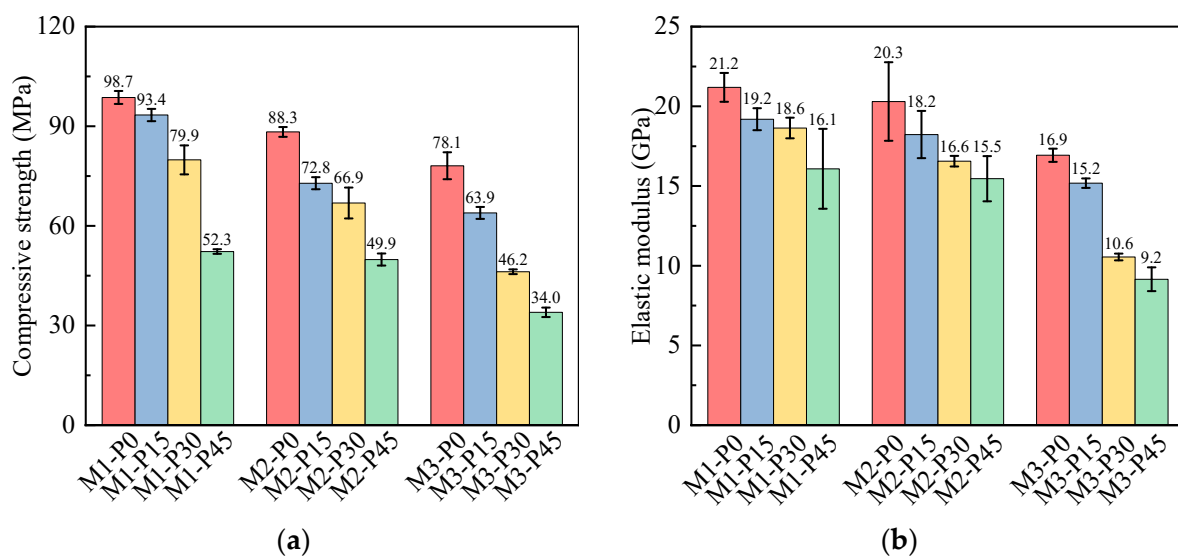


Figure 10. Effect of FA/GGBS ratio and PET powder content on compressive properties: (a) compressive strength, (b) elastic modulus.

Meanwhile, it can be seen from Figure 10 that with the increase in the FA/GGBS ratio, both the compressive strength and elastic modulus of the HDAAC showed a decreasing trend. Compared to M1-P0, the compressive strength of M2-P0 and M3-P0 decreased by 10.4% and 20.6%, respectively, while the elastic modulus decreased by 4.2% and 20.3%, respectively. The reasons for this phenomenon have been discussed in detail in previous studies. It occurred because the increasing slag content resulted in more gel products (i.e., C-A-S-H gel), which reduced the porosity of the HDAAC and made their microstructure denser, thereby leading to higher compressive strength and elastic moduli [49].

Table 4. Compressive properties of HDAAC.

Mix	Compressive Strength (MPa)	Elastic Modulus (GPa)
M1-P0	98.7 (1.9)	21.2 (0.9)
M1-P15	93.4 (1.9)	19.2 (0.7)
M1-P30	79.9 (4.3)	18.6 (0.6)
M1-P45	52.3 (0.7)	16.1 (2.5)
M2-P0	88.3 (1.5)	20.3 (2.5)
M2-P15	72.8 (1.8)	18.2 (1.5)
M2-P30	66.9 (4.7)	16.6 (0.3)
M2-P45	49.9 (1.8)	15.5 (1.4)
M3-P0	78.1 (4.1)	16.9 (0.4)
M3-P15	63.9 (1.8)	15.2 (0.3)
M3-P30	46.2 (0.7)	10.6 (0.2)
M3-P45	34.0 (1.4)	9.2 (0.7)

Note: The values in parentheses represent the standard deviation.

4.2. Tensile Behavior

4.2.1. Failure Mode

Figure 11 shows the failure mode of the HDAAC dumbbell-shaped specimens. Initially, there were no significant changes until the load reached the cracking stress of the HDAAC, where the first crack appeared. With the increasing tensile load, benefitting from the strong fiber bridging between the PE fibers and the matrix, cracks propagated successively. Eventually, the main crack formed in the middle of the specimen and penetrated it upon failure. Regardless of the PET powder content and FA/GGBS ratio, all specimens exhibited multi-cracking and stable cracking behavior during tensile testing, with the cracks mainly concentrating in the middle of the specimens. Dense cracks were also observed outside the measurement area. Increased PET powder content and a larger FA/GGBS ratio resulted in finer surface cracks on the specimens, which maintained good integrity even upon final failure. These observations demonstrate the excellent crack control and deformation capabilities of HDAAC, making them suitable for use in structures with strict crack control requirements.

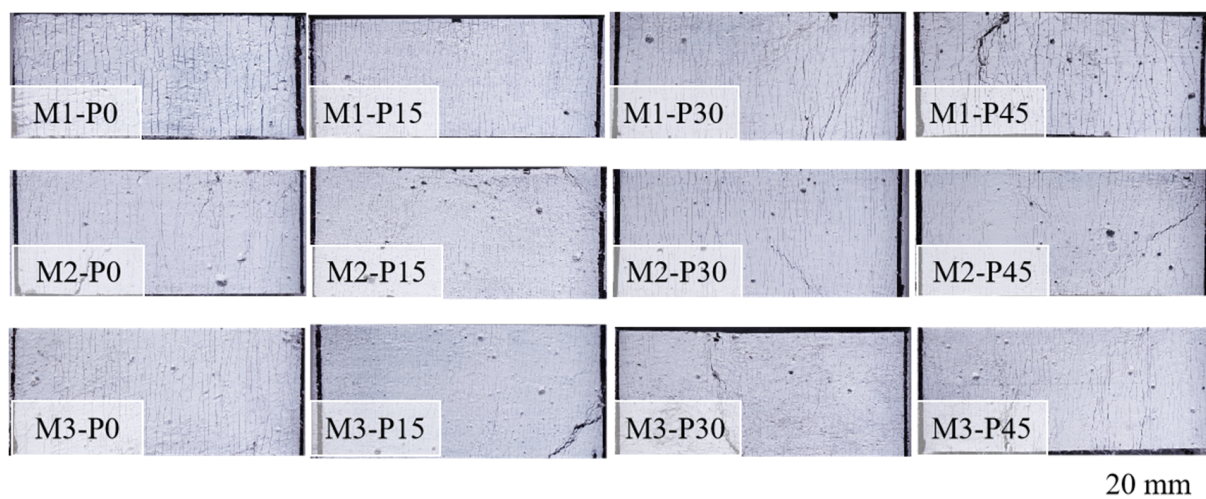


Figure 11. Failure mode of HDAAC under axial tension.

4.2.2. Tensile Stress–Strain Curves

Figure 12 depicts the axial tensile stress–strain curve of the HDAAC, showing typical pseudo-strain-hardening behavior similar to HDC. It can be divided into three stages: linear elastic, pseudo-strain hardening, and strain softening. Initially, the HDAAC's strain

increased slowly but with a rapid stress rise until the cracking stress was reached, where the stress first decreased, deemed the initial cracking strength. Due to the strong bridging between the PE fibers and the matrix, the stress continued to increase, with subsequent crack surface openings causing a stress reduction. This process continued until the ultimate tensile stress and strain were reached, termed the tensile strength and ultimate tensile strain of the HDAAC, accompanied by continuous cracking and expansion, exhibiting significant pseudo-strain-hardening behavior. Eventually, the fibers began to pull out or fracture with a decrease in stress, entering the strain-softening stage.

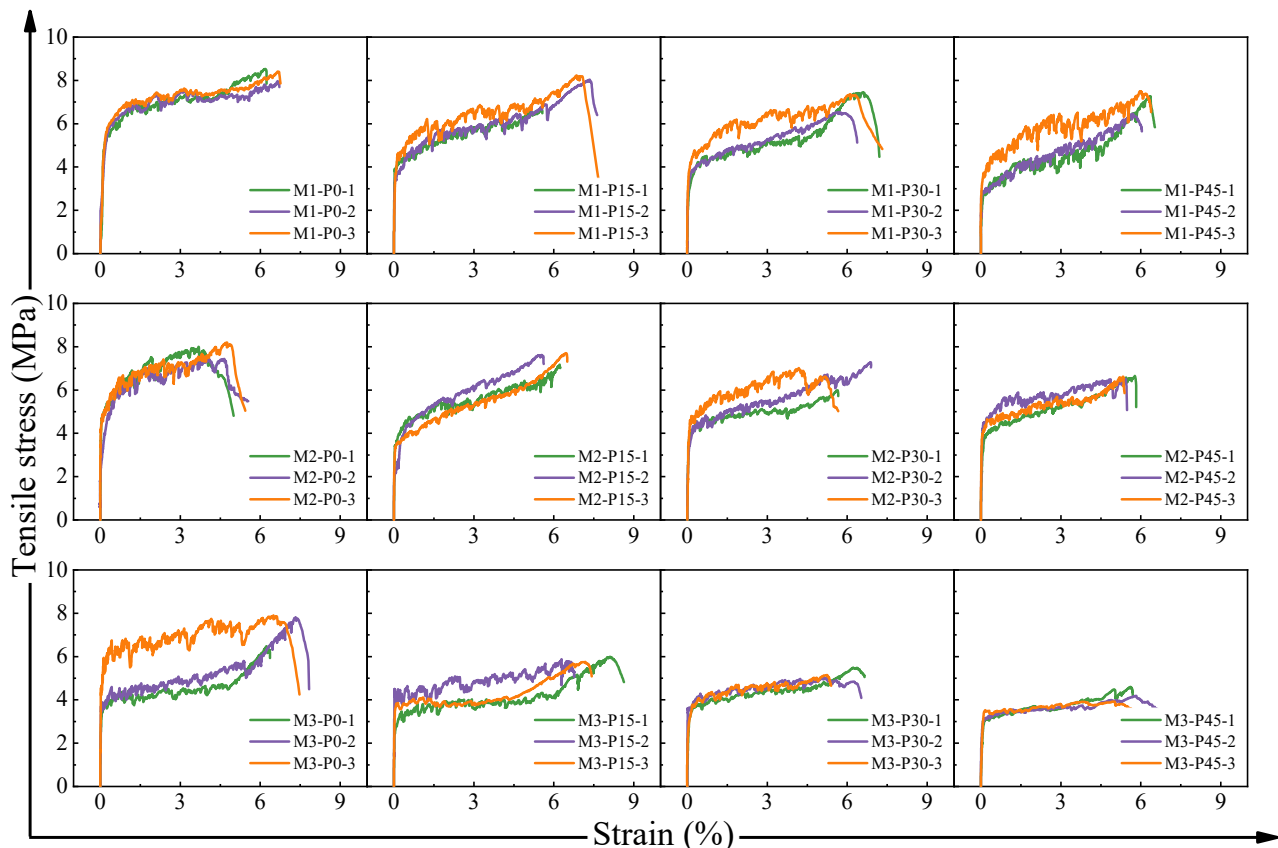


Figure 12. Stress–strain curves of HDAAC under axial tension.

Additionally, the strain-hardening stage exhibited significant stress fluctuations, which are unfavorable for structural stability [50]. Generally, these stress fluctuations are related to the matrix's fracture toughness, the physical properties of the fibers themselves (such as hydrophilicity or hydrophobicity), and their bonding properties with the matrix. As shown in Figure 12, increasing the PET powder content and FA/BBFS ratio was conducive to reducing the stress fluctuations. Nevertheless, it is worth noting that excessive PET powder content is not beneficial for the control of stress fluctuations in HDAAC and may even reduce their ultimate tensile strain.

4.2.3. Tensile Strength and Ultimate Tensile Strain

Figure 13 primarily displays the effects of different FA/GGBS ratios and PET powder content on the tensile parameters of HDAAC. Moreover, the detailed tensile properties of the HDAAC are shown in Table 5. Generally, under a fixed FA/GGBS ratio, increasing the PET powder content led to a decline in both the initial cracking strength and the tensile strength of the HDAAC. Conversely, the ultimate tensile strain of the HDAAC showed a slight increase at lower content. The initial cracking strength, tensile strength, and ultimate tensile strain ranged from 3.0 MPa to 4.6 MPa, 4.2 MPa to 8.2 MPa, and 4.1% to 7.2%, respectively. Compared to M2-P0, the initial cracking strength and tensile strength

of M2-P45 decreased by 17.9% and 15.4%, while the ultimate tensile strain increased by 34.1%. Overall, compared to that without PET powder, the maximum reduction in the initial cracking strength and tensile strength of the HDAAC reached 30.4% and 43.2%, respectively. Moreover, the maximum increase in the initial cracking strength and tensile strength reached 48.8%.

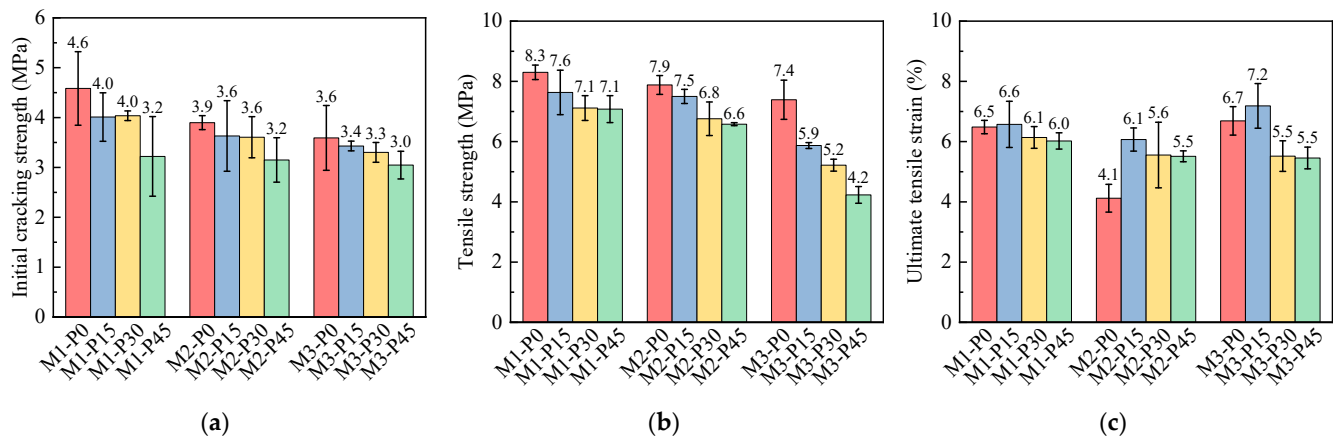


Figure 13. Effects of FA/GGBS ratio and PET powder content on tensile properties: (a) initial cracking strength, (b) tensile strength, (c) ultimate tensile strain.

Table 5. Tensile properties of HDAAC.

Mix	Initial Cracking Strength (MPa)	Tensile Strength (MPa)	Ultimate Tensile Strain (%)
M1-P0	4.6 (0.7)	8.3 (0.2)	6.5 (0.2)
M1-P15	4.0 (0.5)	7.6 (0.7)	6.6 (0.8)
M1-P30	4.0 (0.1)	7.1 (0.4)	6.1 (0.4)
M1-P45	3.2 (0.8)	7.1 (0.4)	6.0 (0.3)
M2-P0	3.9 (0.1)	7.8 (0.3)	4.1 (0.5)
M2-P15	3.6 (0.7)	7.5 (0.2)	6.1 (0.4)
M2-P30	3.6 (0.4)	6.8 (0.6)	5.6 (1.1)
M2-P45	3.2 (0.4)	6.6 (0.0)	5.5 (0.2)
M3-P0	3.6 (0.7)	7.4 (0.7)	6.7 (0.5)
M3-P15	3.4 (0.1)	5.9 (0.1)	7.2 (0.7)
M3-P30	3.3 (0.2)	5.2 (0.2)	5.5 (0.5)
M3-P45	3.0 (0.3)	4.2 (0.3)	5.5 (0.4)

Note: The values in parentheses represent the standard deviation.

According to existing research, parameters such as the initial cracking strength, tensile strength, and ultimate tensile strain of HDC-like materials depend on the fracture toughness of the HDC matrix and the fiber/matrix interface properties. Typically, the initial cracking strength correlates positively with the former, while the tensile strength and ultimate tensile strain rely on both of the properties mentioned above. A matrix with excessive fracture toughness and overly strong fiber/matrix bonding may result in the premature fracture of fibers, leading to the early failure of HDC. Conversely, it favors HDC's ductility.

Considering PET powder's smooth surface and weak bonding with the surrounding matrix, akin to other aggregates like rubber powder and hollow microspheres, its introduction was expected to reduce the matrix's fracture toughness, thereby decreasing the initial cracking strength while enhancing the ultimate tensile strain [12,50].

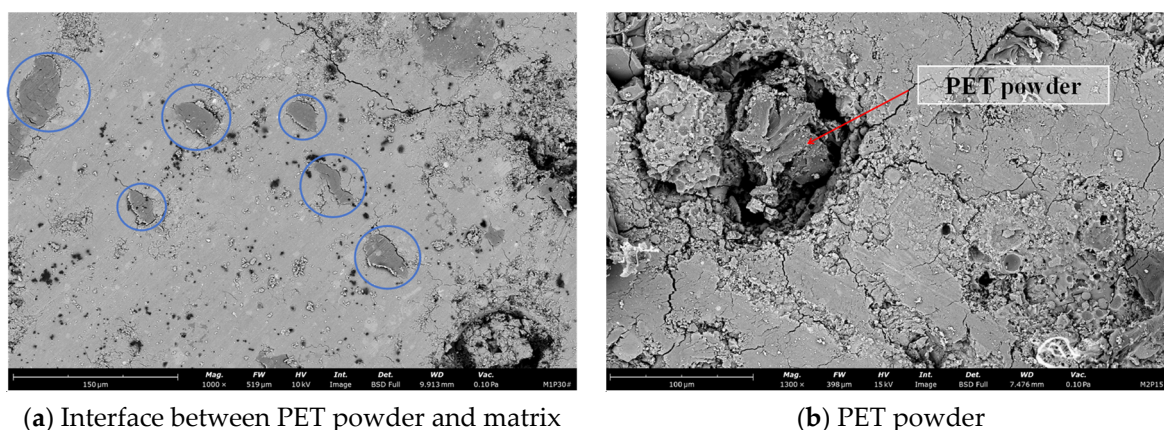
However, as observed in Figure 13, the tensile strength of each group decreased significantly with higher PET powder replacement rates, suggesting that excessive PET powder may weaken the fiber/matrix bridging strength. Regarding the ultimate tensile strain, its decline is attributed to the simultaneous weakening of both the matrix's fracture toughness

and the fiber/matrix bridging strength. However, at higher PET powder replacement rates, finer cracks were observed, which are advantageous for building structures, despite the decrease in the actual ultimate tensile strain values.

Additionally, Figure 13 indicates that higher GGBS content (a lower FA/GGBS ratio) leads to increased tensile strength in HDAAC, attributed to the increased formation of C-A-S-H and C-S-H products with higher GGBS content.

4.3. Microstructure

Figure 14 illustrates the microscopic morphology of the PET powder itself and its interface with the surrounding matrix, as observed under scanning electron microscopy (SEM). At approximately 1000-times magnification, gaps between PET powder and the surrounding matrix were visible, as depicted in Figure 14a. This was attributed to the hydrophobic nature of the PET powder, resulting in poor bonding with the surrounding matrix. Further magnification revealed a distinct interfacial transition zone (ITZ) near the PET powder in the SEM image (Figure 14b). Conversely, the QP exhibited a tendency to bond well with the alkali-activated matrix, as demonstrated in studies by Shi and Xie [51] and Pacheco-Torgal et al. [52]. The variation in the interfacial behavior between the PET powder and QP can be used to interpret the variation in the mechanical performance of the HDAAC mentioned above.



(a) Interface between PET powder and matrix

(b) PET powder

Figure 14. SEM images of HDAAC.

5. Conclusions

In this study, high-ductility alkali-activated composites with recycled polyethylene terephthalate powder (HDAAC) were developed. The axial compressive and tensile properties of the HDAAC were experimentally investigated with varying PET powder replacement ratios and precursor ratios (FA/GGBS ratios). Scanning electron microscopy was employed to verify the influence of the PET powder on the experimental results from a microscopic perspective. This paper primarily discussed the failure modes, stress-strain curves, and corresponding mechanical characteristic parameters of HDAAC under axial compression and tension loads. The main conclusions obtained from this study are as follows.

- (1) The compressive strength and elastic modulus of HDAAC ranged from 34.0 MPa to 98.7 MPa and 9.2 GPa to 21.2 GPa, with specimens exhibiting relatively good integrity after axial compression failure due to the bridging action of PE fibers. The adoption of PET powder as a replacement for quartz powder reduced the compressive strength and elastic modulus of the HDAAC due to the weak bonding between the PET powder and the surrounding matrix and its inherent flexibility. However, it slightly alleviated the brittleness of the HDAAC under compression conditions. With an increase in the GGBS content (reduction in FA/GGBS), the compressive strength and elastic modulus

- of the HDAAC increased due to the increased formation of the C-A-S-H reaction products, resulting in reduced porosity and a denser microstructure.
- (2) The HDAAC under axial tension exhibited typical multiple-cracking phenomena, with the stress–strain curves showing significant pseudo-strain-hardening behavior. As the PET content and FA/GGBS ratio increased, finer surface cracks were observed on the HDAAC specimens, indicating excellent crack control and deformation capabilities. This suggested that the HDAAC developed in this study are highly suitable for use in building structures with strict requirements for crack control.
 - (3) With an increase in the PET content, both the initial cracking strength and tensile strength of the HDAAC generally decreased. Conversely, the ultimate tensile strain of the HDAAC slightly increased at low content. The initial cracking strength, tensile strength, and ultimate tensile strain ranged from 3.0 MPa to 4.6 MPa, 4.2 MPa to 8.2 MPa, and 4.1% to 7.2%, respectively. Overall, compared to that without PET powder, the maximum reduction in the initial cracking strength and tensile strength of the HDAAC reached 30.4% and 43.2%, respectively. Moreover, the maximum increase in the initial cracking strength and tensile strength reached 48.8%. The introduction of PET powder reduced the fracture toughness of the matrix, thereby lowering the initial cracking strength but improving the ultimate tensile strain. Excessive PET powder may weaken the fiber/matrix bridging strength. Higher content of GGBS (lower FA/GGBS) resulted in an increase in the tensile strength of HDAAC due to the increased formation of the C-A-S-H and C-S-H reaction products.
 - (4) The observation of the microscopic morphology of the HDAAC under scanning electron microscopy revealed that, due to the hydrophobic nature of PET powder, a distinct ITZ was present near the PET powder, resulting in poor bonding with the alkali-activated matrix. In contrast, QP dissolved on the surface in a highly alkaline environment, forming better interface properties with the alkali-activated matrix. The different interface properties between the PET powder and QP with the surrounding matrix led to variations in the mechanical properties of the HDAAC.

Author Contributions: Conceptualization, F.M.; methodology, F.M.; formal analysis, S.L.; investigation, J.S. and J.Z.; resources, Y.G.; data curation, C.Z. and J.Z.; writing—original draft preparation, F.M.; writing—review and editing, Y.G.; visualization, L.X. and Y.D.; funding acquisition, Y.G. All authors have read and agreed to the published version of the manuscript.

Funding: This research was funded by the Zhongshan Power Supply Bureau, Guangdong Power Grid Co., Ltd., China Southern Power Grid Co., Ltd., grant number 0320002023030103WL00155.

Data Availability Statement: The data presented in this study are available on request from the corresponding author. The data are not publicly available due to confidentiality issues.

Conflicts of Interest: The authors Fei Meng, Shen Luo, Jingxian Sun, Cheng Zhang, Leilei Xu, and Yankun Du were employed by the Zhongshan Power Supply Bureau, Guangdong Power Grid Co., Ltd. and China Southern Power Grid Co., Ltd. The remaining authors declare that the research was conducted in the absence of any commercial or financial relationships that could be construed as a potential conflict of interest. The authors declare that this study received funding from the Zhongshan Power Supply Bureau, Guangdong Power Grid Co., Ltd. and China Southern Power Grid Co., Ltd. The funders were not involved in the study design; the collection, analysis, or interpretation of the data; the writing of this article; or the decision to submit it for publication.

References

1. Cai, Y.-J.; Xie, Z.-H.; Xiao, S.-H.; Huang, Z.-R.; Lin, J.-X.; Guo, Y.-C.; Zhuo, K.-X.; Huang, P.-y. An investigation of fatigue behavior and residual strength model of steel-GFRP composite bar. *Compos. Struct.* **2024**, *327*, 117685. [[CrossRef](#)]
2. Lin, J.-X.; Huang, P.-Y.; Guo, Y.-C.; Guo, X.-Y.; Zeng, J.-J.; Zhao, C.; Chen, Z.-B. Fatigue behavior of RC beams strengthened with CFRP laminate under hot-wet environments and vehicle random loads coupling. *Int J Fatigue* **2020**, *131*, 105329. [[CrossRef](#)]
3. Romualdi, J.P.; Batson, G.B. Mechanics of Crack Arrest in Concrete. *J. Eng. Mech. Div.* **1963**, *89*, 147–168. [[CrossRef](#)]
4. Lin, J.-X.; Song, Y.; Xie, Z.-H.; Guo, Y.-C.; Yuan, B.; Zeng, J.-J.; Wei, X. Static and dynamic mechanical behavior of engineered cementitious composites with PP and PVA fibers. *J. Build. Eng.* **2020**, *29*, 101097. [[CrossRef](#)]

5. Sahmaran, M.; Yücel, H.E.; Yildirim, G.; Al-Emam, M.; Lachemi, M. Investigation of the Bond between Concrete Substrate and ECC Overlays. *J. Mater. Civ. Eng.* **2014**, *26*, 167–174. [[CrossRef](#)]
6. Yu, K.-Q.; Lu, Z.-D.; Dai, J.-G.; Shah, S.P. Direct Tensile Properties and Stress–Strain Model of UHP-ECC. *J. Mater. Civ. Eng.* **2020**, *32*, 04019334. [[CrossRef](#)]
7. Chen, Z.; Huang, L.; Huang, P.; Xie, J. Axial-Impact Resistance of CFRP-Confined Ultrahigh-Performance Concrete. *J. Compos. Constr.* **2022**, *26*, 04022059. [[CrossRef](#)]
8. Lin, J.-X.; Su, J.-Y.; Pan, H.-S.; Peng, Y.-Q.; Guo, Y.-C.; Chen, W.-S.; Sun, X.-L.; Yuan, B.-X.; Liu, G.-T.; Lan, X.-W. Dynamic compression behavior of ultra-high performance concrete with hybrid polyoxymethylene fiber and steel fiber. *J. Mater. Res. Technol.* **2022**, *20*, 4473–4486. [[CrossRef](#)]
9. Zhuo, K.-X.; Cai, Y.-J.; Lai, H.-M.; Chen, Z.-B.; Guo, Y.-C.; Chen, G.; Xiao, S.-H.; Lan, X.-W. Axial compressive behavior of environmentally friendly high-strength concrete: Effects of recycled tire steel fiber and rubber powder. *J. Build. Eng.* **2023**, *76*, 107092. [[CrossRef](#)]
10. Li, V.C.; Mishra, D.K.; Wu, H. Matrix design for pseudo-strain-hardening fibre reinforced cementitious composites. *Mater. Struct.* **1995**, *28*, 586–595. [[CrossRef](#)]
11. Li, V.C.; Leung, C.K. Steady state and multiple cracking of short random fiber composites. *J. Eng. Mech.* **1992**, *118*, 2246–2264. [[CrossRef](#)]
12. Su, J.-y.; Chen, G.; Pan, H.-s.; Lin, J.-X.; Zhang, J.; Zhuo, K.-x.; Chen, Z.-b.; Guo, Y.-c. Rubber modified high strength-high ductility concrete: Effect of rubber replacement ratio and fiber length. *Constr. Build. Mater.* **2023**, *404*, 133243. [[CrossRef](#)]
13. Wang, B.; Xu, S.; Liu, F. Evaluation of tensile bonding strength between UHTCC repair materials and concrete substrate. *Constr. Build. Mater.* **2016**, *112*, 595–606. [[CrossRef](#)]
14. Su, J.-Y.; Luo, R.-H.; Chen, Z.-B.; Lin, J.-X.; Huang, P.-Y.; Guo, Y.-C. Experimental study on the fracture performance of rubberized high strength-high ductility concrete with J-integral method. *Constr. Build. Mater.* **2024**, *421*, 135668. [[CrossRef](#)]
15. Taylor, M.; Tam, C.; Gielen, D. *Energy Efficiency and CO₂ Emissions from the Global Cement Industry*; IEA: Paris, France, 2006.
16. Hans, K. Cement and process of making the same. U.S. Patent 1591662A, 6 July 1926.
17. Provis, J.L.; van Deventer, J.S.J. *Alkali Activated Materials: State-of-the-Art Report, RILEM TC 224-AAM*; Springer: Berlin/Heidelberg, Germany, 2014.
18. Sun, B.; Sun, Y.; Ye, G.; De Schutter, G. A mix design methodology of blast furnace slag and fly ash-based alkali-activated concrete. *Cem. Concr. Compos.* **2023**, *140*, 105076. [[CrossRef](#)]
19. Lao, J.-C.; Huang, B.-T.; Fang, Y.; Xu, L.-Y.; Dai, J.-G.; Shah, S.P. Strain-hardening alkali-activated fly ash/slag composites with ultra-high compressive strength and ultra-high tensile ductility. *Cem. Concr. Res.* **2023**, *165*, 107075. [[CrossRef](#)]
20. Shubbar, A.A.; Sadique, M.; Kot, P.; Atherton, W. Future of clay-based construction materials—A review. *Constr. Build. Mater.* **2019**, *210*, 172–187. [[CrossRef](#)]
21. Chen, G.; Zheng, D.-P.; Chen, Y.-W.; Lin, J.-X.; Lao, W.-J.; Guo, Y.-C.; Chen, Z.-B.; Lan, X.-W. Development of high performance geopolymer concrete with waste rubber and recycle steel fiber: A study on compressive behavior, carbon emissions and economical performance. *Constr. Build. Mater.* **2023**, *393*, 131988. [[CrossRef](#)]
22. Adam, A.A. Strength and Durability Properties of Alkali Activated Slag and Fly Ash-Based Geopolymer Concrete. Ph.D. Thesis, RMIT University, Melbourne, Australia, 2009.
23. Kumar, S.; Sekhar Das, C.; Lao, J.; Alrefaei, Y.; Dai, J.-G. Effect of sand content on bond performance of engineered geopolymer composites (EGC) repair material. *Constr. Build. Mater.* **2022**, *328*, 127080. [[CrossRef](#)]
24. Lee, S.K.; Oh, T.; Banthia, N.; Yoo, D.-Y. Optimization of fiber aspect ratio for 90 MPa strain-hardening geopolymer composites (SHGC) with a tensile strain capacity over 7.5%. *Cem. Concr. Compos.* **2023**, *139*, 105055. [[CrossRef](#)]
25. Nguyễn, H.H.; Lương, Q.-H.; Choi, J.-I.; Ranade, R.; Li, V.C.; Lee, B.Y. Ultra-ductile behavior of fly ash-based engineered geopolymer composites with a tensile strain capacity up to 13.7%. *Cem. Concr. Compos.* **2021**, *122*, 104133. [[CrossRef](#)]
26. Pan, H.; Xie, Z.; Chen, G.; Su, J.; Zhuo, K.; Chen, Z.; Lin, J.; Feng, C.; Guo, Y. Dynamic compressive behavior of high-strength engineered geopolymer composites. *J. Build. Eng.* **2023**, *80*, 108036. [[CrossRef](#)]
27. Peng, Y.-Q.; Zheng, D.-P.; Pan, H.-S.; Yang, J.-L.; Lin, J.-X.; Lai, H.-M.; Wu, P.-Z.; Zhu, H.-Y. Strain hardening geopolymer composites with hybrid POM and UHMWPE fibers: Analysis of static mechanical properties, economic benefits, and environmental impact. *J. Build. Eng.* **2023**, *76*, 107315. [[CrossRef](#)]
28. Zhong, H.; Zhang, M. Engineered geopolymer composites: A state-of-the-art review. *Cem. Concr. Compos.* **2023**, *135*, 104850. [[CrossRef](#)]
29. Lin, J.-X.; Liu, R.-A.; Liu, L.-Y.; Zhuo, K.-Y.; Chen, Z.-B.; Guo, Y.-C. High-strength and high-toughness alkali-activated composite materials: Optimizing mechanical properties through synergistic utilization of steel slag, ground granulated blast furnace slag, and fly ash. *Constr. Build. Mater.* **2024**, *422*, 135811. [[CrossRef](#)]
30. Belmokaddem, M.; Mahi, A.; Senhadji, Y.; Pekmezci, B.Y. Mechanical and physical properties and morphology of concrete containing plastic waste as aggregate. *Constr. Build. Mater.* **2020**, *257*, 119559. [[CrossRef](#)]
31. Ibrahim, O.M.O.; Tayeh, B.A. Combined effect of lightweight fine aggregate and micro rubber ash on the properties of cement. *Adv. Concr. Constr.* **2020**, *10*, 537–546.
32. Guo, Y.-C.; Li, X.-M.; Zhang, J.; Lin, J.-X. A review on the influence of recycled plastic aggregate on the engineering properties of concrete. *J. Build. Eng.* **2023**, *79*, 107787. [[CrossRef](#)]

33. Hama, S.M.; Hilal, N.N. Fresh properties of self-compacting concrete with plastic waste as partial replacement of sand. *Int. J. Sustain. Built Environ.* **2017**, *6*, 299–308. [[CrossRef](#)]
34. Akçaözöğlü, S.; Ulu, C. Recycling of waste PET granules as aggregate in alkali-activated blast furnace slag/metakaolin blends. *Constr. Build. Mater.* **2014**, *58*, 31–37. [[CrossRef](#)]
35. Hannawi, K.; Kamali-Bernard, S.; Prince, W. Physical and mechanical properties of mortars containing PET and PC waste aggregates. *Waste Manag.* **2010**, *30*, 2312–2320. [[CrossRef](#)] [[PubMed](#)]
36. Kou, S.C.; Lee, G.; Poon, C.S.; Lai, W.L. Properties of lightweight aggregate concrete prepared with PVC granules derived from scraped PVC pipes. *Waste Manag.* **2009**, *29*, 621–628. [[CrossRef](#)] [[PubMed](#)]
37. Faraj, R.H.; Sherwani, A.F.H.; Daraei, A. Mechanical, fracture and durability properties of self-compacting high strength concrete containing recycled polypropylene plastic particles. *J. Build. Eng.* **2019**, *25*, 100808. [[CrossRef](#)]
38. Saleem, S.; Pimanmas, A.; Qureshi, M.I.; Rattanapitikon, W. Axial Behavior of PET FRP-Confined Reinforced Concrete. *J. Compos. Constr.* **2021**, *25*, 04020079. [[CrossRef](#)]
39. ASTM C469/C469M-22; Standard Test Method for Static Modulus of Elasticity and Poisson's Ratio of Concrete in Compression. ASTM International: West Conshohocken, PA, USA, 2022.
40. Yokota, H.; Rokugo, K.; Sakata, N. JSCE Recommendations for design and construction of high performance fiber reinforced cement composite with multiple fine cracks. In *High Performance Fiber Reinforced Cement Composites*; Springer: Tokyo, Japan, 2007.
41. Chen, W.F.; Saleeb, A.F. *Constitutive Equations for Materials of Concrete and Soil*; Yu, T.I.-Q., Wu, X.-W., Liu, X.-L., Han, D.-J., Eds.; China Architecture & Building Press: Beijing, China, 2004.
42. Ding, Y.; Yu, J.-t.; Yu, K.-Q.; Xu, S.-l. Basic mechanical properties of ultra-high ductility cementitious composites: From 40 MPa to 120 MPa. *Compos. Struct.* **2018**, *185*, 634–645. [[CrossRef](#)]
43. Frigione, M. Recycling of PET bottles as fine aggregate in concrete. *Waste Manag.* **2010**, *30*, 1101–1106. [[CrossRef](#)] [[PubMed](#)]
44. Guo-Hao, F. Multiscale Characterisation of Microstructure and Mechanical Properties of Alkali-Activated Fly Ash-Slag Concrete. Ph.D. Thesis, University College, London, UK, 2021.
45. Lazorenko, G.; Kasprzhitskii, A.; Fini, E.H. Polyethylene terephthalate (PET) waste plastic as natural aggregate replacement in geopolymer mortar production. *J. Clean. Prod.* **2022**, *375*, 134083. [[CrossRef](#)]
46. Bamigboye, G.; Tarverdi, K.; Adigun, D.; Daniel, B.; Okorie, U.; Adediran, J. An appraisal of the mechanical, microstructural, and thermal characteristics of concrete containing waste PET as coarse aggregate. *Clean. Waste Syst.* **2022**, *1*, 100001. [[CrossRef](#)]
47. Rahmani, E.; Dehestani, M.; Beygi, M.H.A.; Allahyari, H.; Nikbin, I.M. On the mechanical properties of concrete containing waste PET particles. *Constr. Build. Mater.* **2013**, *47*, 1302–1308. [[CrossRef](#)]
48. García-Lodeiro, I.; Fernández-Jiménez, A.; Palomo, A. Variation in hybrid cements over time. Alkaline activation of fly ash-portland cement blends. *Cem. Concr. Res.* **2013**, *52*, 112–122. [[CrossRef](#)]
49. Nath, P.; Sarker, P.K. Flexural strength and elastic modulus of ambient-cured blended low-calcium fly ash geopolymer concrete. *Constr. Build. Mater.* **2017**, *130*, 22–31. [[CrossRef](#)]
50. Zhou, Y.; Xi, B.; Sui, L.; Zheng, S.; Xing, F.; Li, L. Development of high strain-hardening lightweight engineered cementitious composites: Design and performance. *Cem. Concr. Compos.* **2019**, *104*, 103370. [[CrossRef](#)]
51. Shi, C.; Xie, P. Interface between cement paste and quartz sand in alkali-activated slag mortars. *Cem. Concr. Res.* **1998**, *28*, 887–896. [[CrossRef](#)]
52. Pacheco-Torgal, F.; Castro-Gomes, J.; Jalali, S. Investigations about the effect of aggregates on strength and microstructure of geopolymeric mine waste mud binders. *Cem. Concr. Res.* **2007**, *37*, 933–941. [[CrossRef](#)]

Disclaimer/Publisher's Note: The statements, opinions and data contained in all publications are solely those of the individual author(s) and contributor(s) and not of MDPI and/or the editor(s). MDPI and/or the editor(s) disclaim responsibility for any injury to people or property resulting from any ideas, methods, instructions or products referred to in the content.